ADVANCED FUNCTIONAL MATERIALS
www.afm-journal.de

Topographically Flat Substrates with Embedded Nanoplasmonic Devices for Biosensing

*Jincy Jose, Luke R. Jordan, Timothy W. Johnson, Si Hoon Lee, Nathan J. Wittenberg, and Sang-Hyun Oh**

The ability to precisely control the topography, roughness, and chemical properties of metallic nanostructures is crucial for applications in plasmonics, nanofluidics, electronics, and biosensing. Here a simple method to produce embedded nanoplasmonic devices that can generate tunable plasmonic fields on ultraflat surfaces is demonstrated. Using a template-stripping technique, isolated metallic nanodisks and wires are embedded in optical epoxy, which is capped with a thin silica overlayer using atomic layer deposition. The top silica surface is topographically flat and laterally homogeneous, providing a uniform, high-quality biocompatible substrate, while the nanoplasmonic architecture hidden underneath creates a tunable plasmonic landscape for optical imaging and sensing. The localized surface plasmon resonance of gold nanodisks embedded underneath flat silica films is used for real-time kinetic sensing of the formation of a supported lipid bilayer and subsequent receptor-ligand binding. Gold nanodisks can also be embedded in elastomeric materials, which can be peeled off the substrate to create flexible plasmonic membranes that conform to non-planar surfaces.

1. Introduction

Engineered metallic nanostructures can harness surface plasmons to tightly localize optical energy below diffraction limits.[1–4] Using top-down fabrication or bottom-up synthesis, the geometry of these nanostructures can be readily tuned, which, in turn, allows tailoring the spatial distribution of plasmonic fields and "hot spots" for applications in sensing,[5–12] spectroscopy,[13] imaging,[4] optical trapping,[14] and data storage.[15] However, lithographically patterned metal films or dispersed metal nanoparticles introduce surface topography as a byproduct, which can profoundly influence how the resulting non-planar surfaces interact with fluids, biomolecules, and particles at the nanoscale.[16,17]

For many applications, it is desirable to create and manipulate plasmonic fields laterally using metallic nanostructures without disrupting the planarity and lateral homogeneity of the active surface. For example, in near-field scanning optical microscopy, sample topography can generate artifacts via tip-sample interactions and obscure the near-field optical information.[18,19] Topography, roughness, and lateral heterogeneity of substrates also impose severe constraints on surface modifications and biological interfacing. Indeed it has been shown that the size, shape, and roughness of gold nanoparticles on a substrate can affect the morphology, spreading, and lateral heterogeneity of the supported lipid bilayer (SLB) membranes formed around them.[20,21] To eliminate the roughness-induced issues in the formation of self-assembled monolayers and lipid bilayer membranes, template-stripped gold films have been employed,[22] but unpatterned gold films cannot be used to tailor localized plasmonic fields. Topographically flat surfaces with ultrasmooth embedded metals can also benefit nanofluidics,[16] 3D device integration,[23] nanophotonic circuitry,[24] and elastomeric electronics.[25]

Despite such widespread demands, planarization of patterned metals remains one of the most difficult and laborious steps in nanofabrication, as exemplified in the damascene process,[26] which is a complex multistep process for planarizing metal interconnects in microprocessors. Here we address the processing challenges in the planarization of metallic patterns and provide a facile technique by combining standard lithography, template stripping, and atomic layer deposition (ALD) to produce ultraflat silica surfaces with nanoplasmonic features buried underneath. The top surface of the embedded metals gives an ultraflat topography with a roughness and step height variation below 1 nm. The patterned surface is then covered with a silica overlayer using ALD,[27,28] which ensures biocompatibility and lateral homogeneity of our structures regardless of the underlying metal structures. Importantly, the silica overlayer grown by ALD is also ultrasmooth (sub-1-nm roughness) and thin (≈10 nm) so as not to bury the optical near-field of the embedded nanoplasmonic structures. Furthermore, the silica layer acts as a spacer to prevent quenching of fluorophores, enabling concurrent plasmonic sensing and fluorescence

Dr. J. Jose, L. R. Jordan, T. W. Johnson, Dr. S. H. Lee, Dr. N. J. Wittenberg, Prof. S.-H. Oh
Laboratory of Nanostructures and Biosensing
Department of Electrical and Computer Engineering
University of Minnesota
Twin Cities, MN 55455, USA
E-mail: sang@umn.edu

L. R. Jordan, Dr. S. H. Lee, Dr. N. J. Wittenberg, Prof. S.-H. Oh
Department of Biomedical Engineering
University of Minnesota
Twin Cities, MN 55455, USA

Prof. S.-H. Oh
Department of Biophysics and Chemical Biology
Seoul National University
Seoul, 151-747, Korea

DOI:10. 1002/adfm.201202214

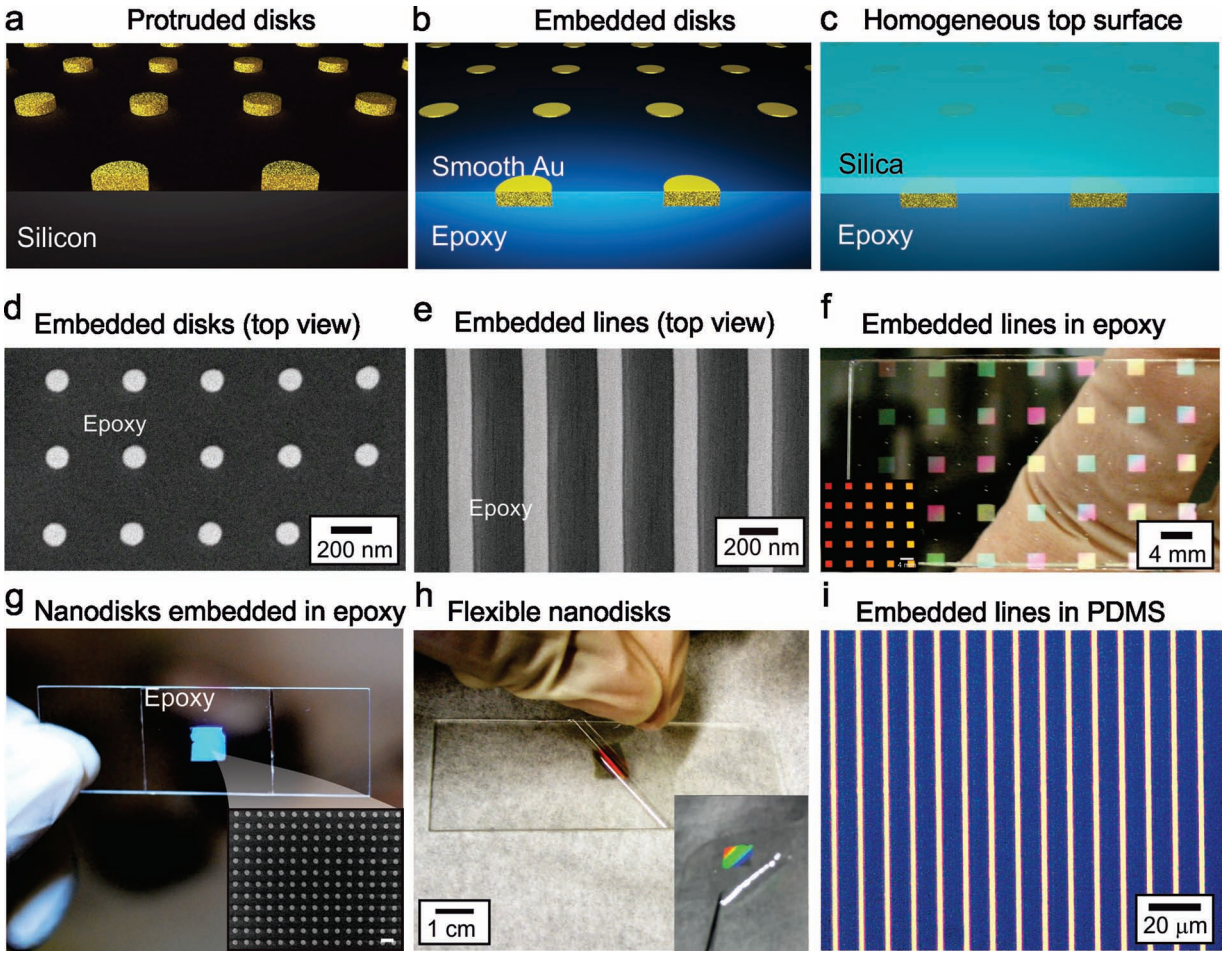

Figure 1. Planar embedded metallic structures. Schematic of a) protruded gold nanodisks on silicon substrate and b) embedded gold nanodisks in epoxy. c) Schematic of homogenous silica layer formed on top of the embedded gold nanodisks. Scanning electron microscopy (SEM) images of 27 nm thick gold d) nanodisks and e) nanowires embedded in epoxy on a glass substrate. f) Photograph of a large area periodic silver line pattern (period 10 µm, line width 1 µm and thickness 200 nm) embedded in epoxy on a glass substrate. Inset shows the line pattern on a silicon substrate before stripping off with epoxy. Photographs of large area (8 mm × 8 mm) Ag nanodisks g) embedded in epoxy (period 500 nm, disk diameter 200 nm and thickness 135 nm) and h) peeled off to form a flexible nanodisk membrane. Inset in (g) shows SEM image of the embedded nanodisks and that in (h) shows the flexible membrane. The scale bar in the inset in (g) is 500 nm. i) Optical microscopy image of the periodic Au line pattern (period 10 µm, line width 1 µm and thickness 200 nm) embedded in PDMS.

imaging, which is useful when measuring the fluidity of lipid membranes or investigating plasmon-enhanced fluorescence. To demonstrate the utility of our method, we fabricate localized surface plasmon resonance (LSPR) biosensors using a periodic array of gold nanodisks buried underneath a silica film, upon which high-quality biomimetic SLB membranes can readily be reconstituted. The LSPR of the embedded gold nanodisks is monitored in real time to measure protein-lipid binding kinetics with a high signal-to-noise ratio.

2. Results and Discussion

2.1. Fabrication of Embedded Nanostructures

Template stripping has been used to produce both unpatterned[29–31] and patterned[26,32–40] metallic films with ultrasmooth surfaces. Instead of peeling off continuous metal films from patterned Si templates, as previously shown,[33,41] here isolated small metallic disks and lines are embedded in planarized media. In particular, peeling off isolated metallic nanodisks from a silicon template demands a strong and uniform adhesion between the embedding layer and the patterns because of the small contact area. At the same time, it should also be possible to peel off the embedding layer from the silicon surface. We show that optical epoxy and poly(dimethylsiloxane) (PDMS) can meet these requirements and produce highly uniform embedded nanostructures over a large area.

Standard lithographic processing on a Si wafer creates disconnected metal patterns (see **Figure 1**a), which are then capped by an adhesive media such as optical epoxy and peeled off, exposing an ultrasmooth planar surface defined by the Si wafer (shown in Figure 1b). See Supporting Information (Figure S1) for the detailed fabrication scheme. It should be noted that a Cr or Ti layer, which is typically used to improve

the adhesion between patterned metals and substrates but also increases unwanted plasmon damping, is not needed in our template-stripping process. Figure 1d,e show scanning electron microscopy (SEM) images of a gold nanodisk array and a gold nanowire array, respectively, embedded in epoxy on a glass substrate. We are able to template-strip gold nanostructures that are as small as 100 nm in width and 27 nm in height. Also, metallic structures over a large area (e.g., periodic Ag lines and nanodisks shown in Figure 1f,h, respectively) can be template-stripped with very high yield. The large-area embedded nanodisk array can be peeled off using a thin epoxy film to produce flexible devices, as shown in Figure 1h, or placed on a glass substrate. To demonstrate the versatility of our fabrication scheme, we also embedded metallic nanostructures in PDMS, which can be useful for applications such as flexible electronics[42] or flexible metamaterials.[43] A periodic Au line pattern (200 nm thick) embedded in PDMS is shown in Figure 1i. The adhesion between PDMS and metal is not as strong as that between metal and optical epoxy. To increase gold-PDMS adhesion, a self-assembled monolayer (3-mercaptopropyl trimethoxysilane) was formed on the gold patterns prior to the addition of the PDMS layer.

2.2. Atomic Force Microscopy on Embedded Nanostructures

We used atomic force microscopy (AFM) to measure the surface profile of embedded metallic nanostructures. Contact-mode AFM height images of 27 nm thick gold nanodisks and nanowires on silicon substrates, before template stripping, are shown in **Figure 2**a,b, respectively. AFM height images of the template-stripped gold nanodisks and nanowires embedded in epoxy are shown in Figure 2c,d, and the measured root-mean-square (r.m.s.) roughness is 0.32 nm and 0.42 nm, respectively. The line scans taken along the black dashed lines in the AFM images of the embedded structures confirm that the surface roughness within each gold and epoxy domain is maintained below 1 nm. Furthermore, the step height at the interface between gold and epoxy is also below 1 nm, because they are cured together while being constrained on a flat silicon wafer. AFM lateral friction images of the embedded structures are shown in Figure S2 in the Supporting Information.

2.3. Atomic Layer Deposition of Silica Overlayer

While the physical topography and roughness are considerably minimized via template stripping, the exposed surface is spatially nonuniform and consists of patterned metals and surrounding epoxy media, complicating subsequent surface modifications or biological interfacing that is required for uniform SLB formation in biomembrane-based sensing applications. It is well known that the formation and mobility of lipids in SLBs and their interactions with other molecules are closely related to the topography, local curvature, and material properties of the underlying substrate.[44] Even if the topography is completely eliminated via template stripping, alternating chemical landscape caused by the exposed metals and dielectric surfaces can lead to lateral heterogeneity and diffusion barriers

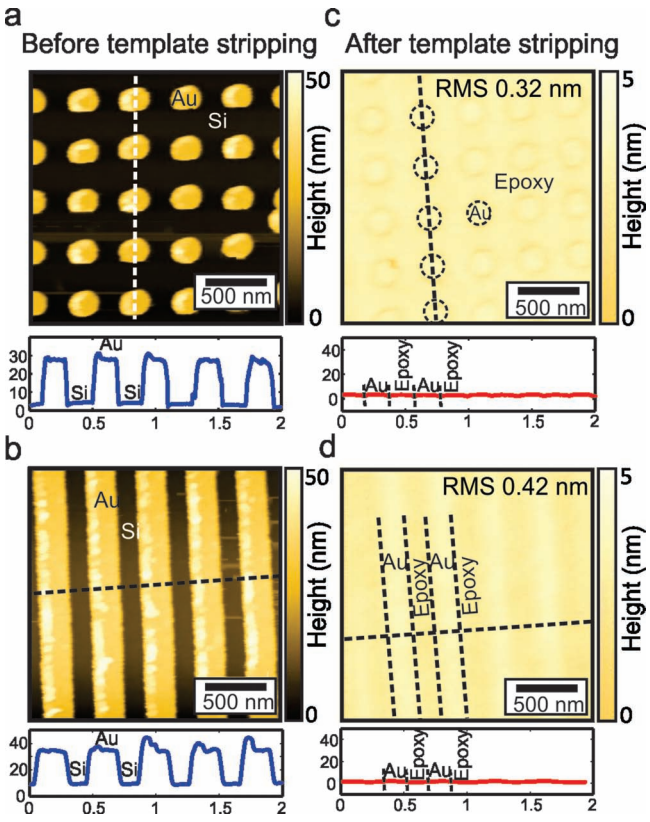

Figure 2. Surface roughness measurements of the gold nanodisks and nanowires. Contact-mode AFM height images of 27 nm thick gold a) nanodisks and b) nanowires deposited on silicon substrate. Line scans, along the black dashed lines in the AFM images, are shown in the bottom panel corresponding to each AFM image. AFM height images of the gold c) nanodisks and d) nanowires embedded in epoxy on a glass substrate.

in the SLBs.[45] These problems can be resolved by coating the template-stripped surface with a thin silica overlayer using ALD (see Figure 1c). A thickness of 10 nm was chosen to ensure the growth of high-quality silica film with no voids and pinholes. After the ALD process, the measured r.m.s. roughness of the top silica surface still remains below 1 nm. For biosensing applications, it can be desirable to work with silica surfaces, which are hydrophilic, biocompatible, and chemically similar to standard microscope slides, rather than modifying gold or silver surfaces with self-assembled monolayers.[7] In particular, it is straightforward to form SLBs on a silica surface,[46,47] whereas the formation of SLBs on a gold surface generally requires modifications with self-assembled monolayers or tethering linkages.[48] Also, embedded metallic nanostructures made of silver can be easily contaminated by oxidation and sulfate formation, which will degrade the sensor performance. Dielectric overlayers deposited by ALD can effectively protect silver nanostructures from such environmental contamination.[49,50] The capability to integrate ultrasmooth silica surfaces with LSPR sensors will also benefit novel applications in membrane biophysics, such as the SLB formation using a shear-driven method, where a lipid bilayer is pushed over the planar surface.[51] The silica overlayer also permits permanent bonding

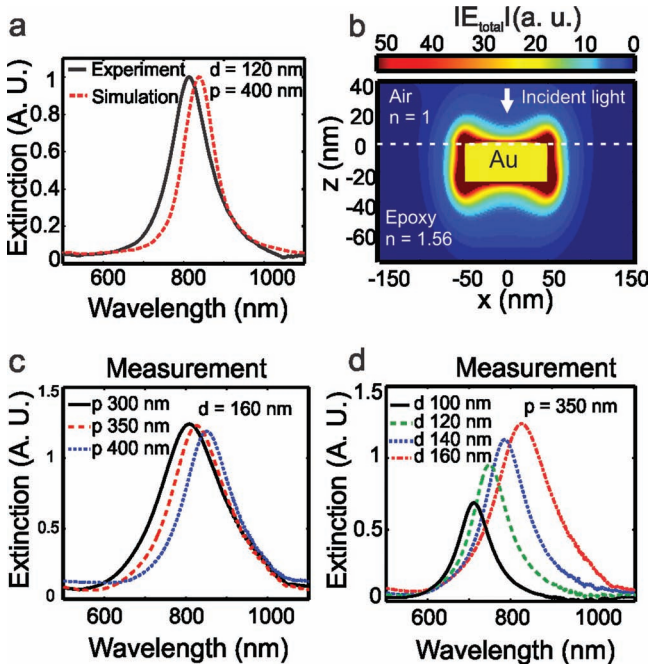

Figure 3. Spectral characteristics of the embedded gold nanodisks for varying period, *p* and disk diameter, *d*. a) Measured extinction spectrum (black solid line) and 3D FDTD simulation (red dashed line) of embedded gold nanodisk array (p = 400 nm and d = 120 nm). Here A. U. refers to absorption units. b) The calculated steady-state time-averaged total electric Þeld intensity (E_{total}). Extinction spectra of the embedded gold nanodisk array for varying c) period (d = 160 nm) and d) disk diameter (p = 350 nm).

of PDMS microfluidic chips, which eliminates leakage during sensing experiments.

2.4. Optical Properties of Embedded Gold Nanodisks

In **Figure 3**a, an experimental extinction spectrum of the embedded gold nanodisk array (period, p = 400 nm and disk diameter, d = 120 nm) is compared with a 3D finite-difference time-domain (FDTD) simulation with periodic boundary conditions. The small discrepancy in the resonance wavelengths in the experimental and the calculated extinction spectra is attributed to the difference in the size and shape of the fabricated nanodisks from the simulated nanodisks as well as the difference in the optical constants of gold used for simulation. Figure 3b shows the calculated steady-state time-averaged total electric field intensity ($E_{total} = E_x^2 + E_y^2 + E_z^2$) at the resonance. The electromagnetic (EM) field is mainly concentrated at the corners of the nanodisk and localized on both the gold-air interface and the gold-epoxy interface.

The LSPR peak of the embedded gold nanodisks shifts toward longer wavelengths with an increasing period (Figure 3c). Figure 3d shows the extinction spectra with fixed period of 350 nm and a range of disk diameters (d = 100, 120, 140 and 160 nm). The interparticle interaction in an array of nanoparticles can be of two types: a near-field coupling (if particles are closely spaced) and a far-field radiative coupling (when the particles are spaced far apart).[52] The most closely spaced nanodisks among our samples have an edge-to-edge distance of 140 nm (period of 300 nm and diameter of 160 nm), which is large for near-field coupling to occur. In the far-field coupling, when a grating order changes from evanescent to radiative, a strong dipolar interaction of the nanodisks' scattered optical fields occurs and the LSPR red-shifts.[38] The red shifts of the LSPR peak with increasing disk diameter and period are attributed to a modification of the plasmon resonances due to the far-field radiative interaction between the nanodisks. The red-shifted LSPR peaks corresponding to the larger periodicity are sharper than those corresponding to the smaller periodicity. For LSPR sensing studies, we have chosen the nanodisk sample with the largest period of 400 nm.

2.5. Characterizing Optical Near-Field of Embedded Nanodisks

The near-field sensing characteristics of a plasmonic sensor are determined by the decay length of the EM field at the sensor surface. We experimentally determined the distance-dependent EM field decay length and the local sensing range above the nanodisks (period 400 nm and diameter 100 nm) using ALD of Al_2O_3 on the embedded nanodisks.[50,53] The optical extinction spectra taken after sequential deposition of 2 nm thick Al_2O_3, up to a thickness of 40 nm, are shown in **Figure 4**a. As shown in Figure 4b, the LSPR shift changes linearly as the Al_2O_3 layer thickness reaches ≈8 nm, and then begins to flatten out beyond 30 nm, because the EM field decays away from the nanodisk surface. The experimental data in Figure 4b is fitted to Equation S1[53] (shown in the Supporting Information) to retrieve an EM field decay length of 20.71 nm ± 2.21 nm, which is in accordance with earlier reported values of 5–15 nm.[54] The short EM field decay length of an LSPR sensor limits its probing range, but improves its sensitivity to thin films or small biomolecules. We determined the local index sensitivity of the embedded nanodisk array in air to be 4.5 nm per nm of Al_2O_3, which shows good agreement with the calculated (FDTD) sensitivity of 4.9 nm per nanometer of Al_2O_3 (shown in Figure 4c). It is interesting to note that, although the nanodisk is completely buried below the sensing medium (see Figure 3b), the measured local index sensitivity of our embedded nanodisk array is still comparable to the measured sensitivity of a nanodisk LSPR sensor with protruding geometry.[55] Also, we observed a decrease in the EM field decay length with decreasing the period of the nanodisk array (not shown), which is attributed to the broader LSPR peak with decreasing period (as shown in Figure 3c). Since the field decay length extends to ≈20 nm, we can still perform real-time biosensing after coating the surface with a 10 nm silica overlayer. We performed FDTD simulations, with thin Al_2O_3 layers, to compare the sensor response of embedded nanodisks with protruded nanodisks (see Figure 4c). As expected, the local index sensitivity of the protruded nanodisks is higher than the embedded nanodisks, since the contact area of the Al_2O_3 layer and the protruded nanodisks is larger.

2.6. Lateral Mobility of SLB on Silica Surface

We determined the lateral mobility of SLBs formed on a template-stripped, planar silica-coated (≈10 nm thick) epoxy

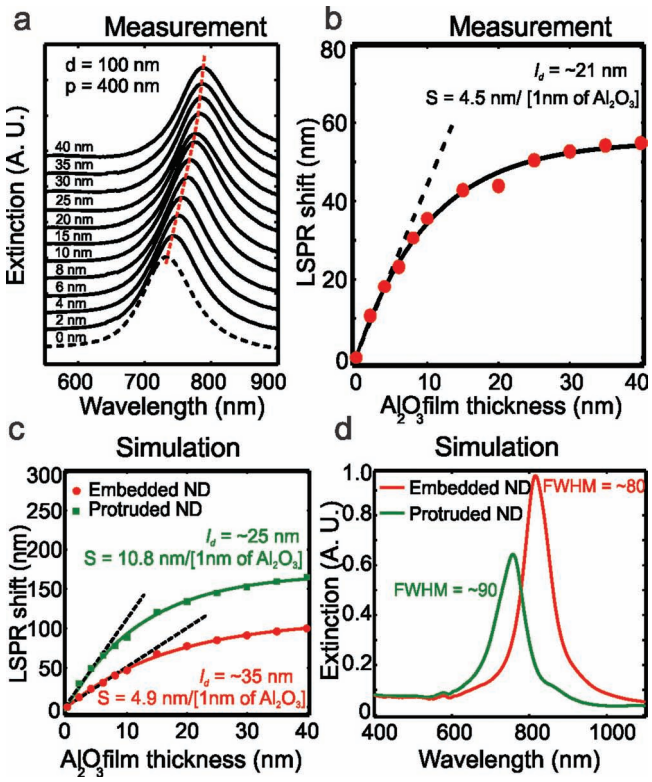

Figure 4. Near-Þeld LSPR sensor response characteristics of the embedded gold nanodisks. a) Extinction spectra (in absorption units) of embedded gold nanodisk array (p = 400 nm and d = 100 nm), for sequential deposition of Al_2O_3 layer. The spectrum taken without Al_2O_3 layer is denoted by a dotted line. The spectra are shifted in y-axis for clarity. The red dashed line is a guide for the eye. b) LSPR shift versus Al_2O_3 layer thickness. The experimental (dot) data is Þtted (dash) using Equation S1 (Supporting Information). c) Simulated sensor responses (in air) of embedded (closed circles) and protruded (closed squares) gold nanodisks (p = 400 nm and d = 100 nm). d) Simulated extinction spectra (in air) of embedded and protruded nanodisks (p = 400 nm and d = 100 nm). ND: nanodisks; S: local index sensitivity; and l_d: Þeld decay length.

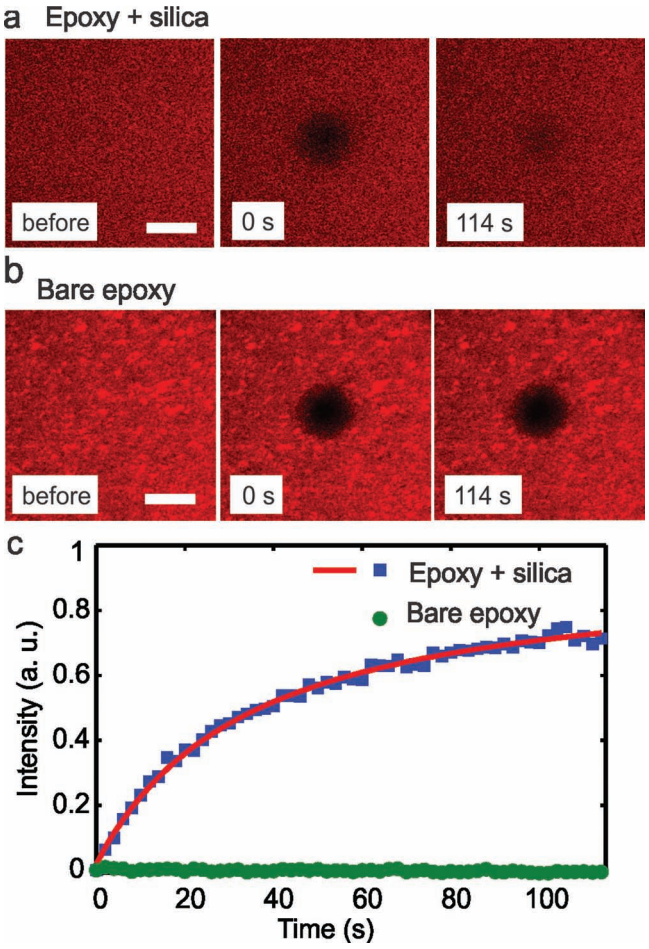

Figure 5. Fluorescence images from a FRAP experiment showing the ßuorescence intensity recovery of a bleached spot on a) a silica-coated (≈10 nm thick) epoxy surface and b) a bare epoxy surface. The images shown are before, directly after and after 114 s of bleaching. The scale bar is 20 µm. c) Average ßuorescence intensity for an SLB over the silica-coated epoxy surface (blue squares) and the bare epoxy surface (green circles). Negligible recovery over the bare epoxy surface points towards the presence of adsorbed intact vesicles, whereas, an ≈93% recovery (at inÞnity) over the silica-coated epoxy surface implies the formation of a SLB on that surface.

surface by performing fluorescence recovery after photobleaching (FRAP) experiments.[56] After vesicle rupture, the substrate was imaged using an upright confocal microscope. The details of the FRAP analysis is given in the Supporting Information. **Figure 5**a,b show the fluorescence images from the FRAP experiment on the silica-coated epoxy surface and a bare epoxy surface, respectively. The images were taken before, directly after, and 114 s after bleaching. Plots of the fluorescence intensity in the bleached area over time for an SLB over the silica-coated epoxy surface and the bare epoxy surface are shown in Figure 5c, along with a fitted curve. An average recovery of 93.1% ± 0.4% of the mean fluorescence intensity is measured on the silica-coated epoxy surface, which is comparable to the recovery of a SLB on a glass surface.[57] The diffusion coefficient for lipids in the SLB is calculated to be 2.06 ± 0.04 µm^2/s. FRAP measurements over the bare epoxy surface (without silica coating) revealed 0% recovery, which indicates that a SLB did not form. Also, the bright areas in Figure 5b are likely clumps of unruptured vesicles.

2.7. LSPR Kinetic Sensing of Protein Binding to Biotinylated SLBs

We used silica-coated planar embedded gold nanodisks as LSPR sensors to measure the formation of SLBs and the binding of a protein, streptavidin-R-phycoerythrin (SAPE), to biotinylated SLBs, as illustrated in **Figure 6**a. A PDMS microfluidic chip with two microfluidic channels was aligned and permanently bonded to the silica-coated embedded nanodisk array (Figure 6b). 1 mM biotinylated vesicles (10 mol% biotin-PE) and 1 mM biotin-free vesicles were injected into channel 1 (Ch 1) and channel 2 (Ch 2), respectively. A sudden rise in the peak shift (indicated by an arrow) is observed upon injecting the vesicles to the channels as shown in Figure 6c. This peak shift indicates vesicle adsorption to the surface and subsequent

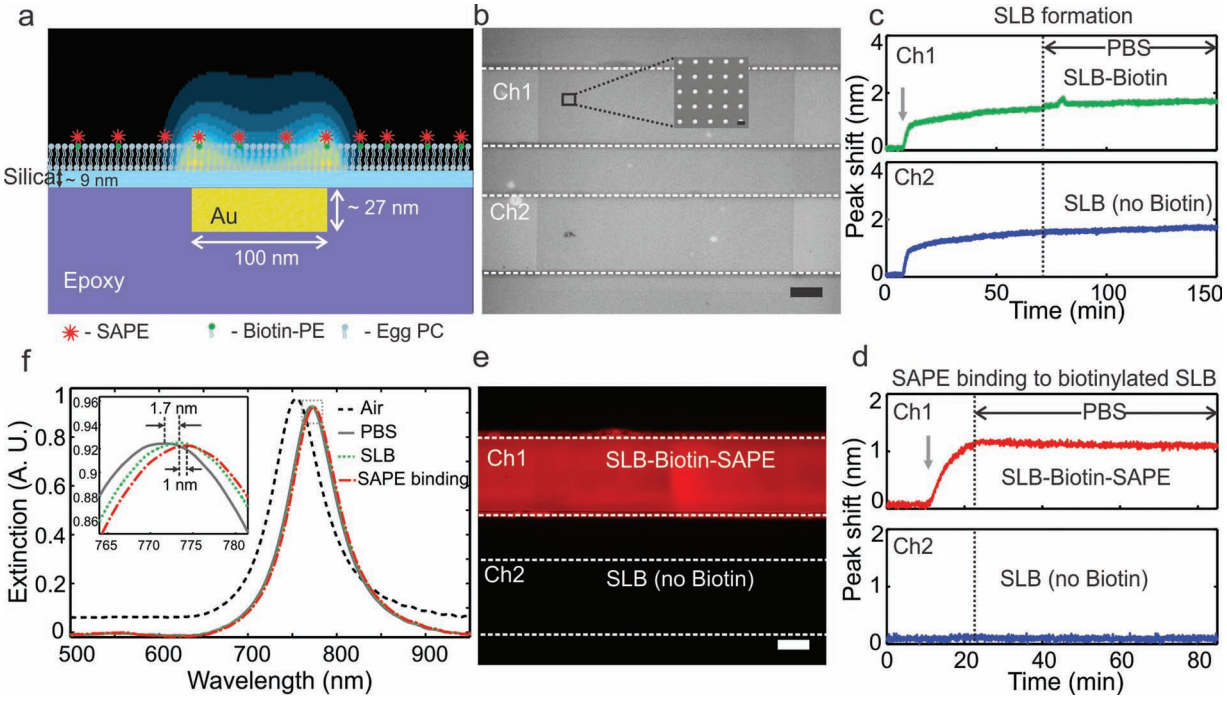

Figure 6. LSPR kinetic sensing of biotinylated SLBs and streptavidin-R-phycoerythrin (SAPE) binding. a) A cartoon depicting the SAPE bound to SLBs functionalized with biotin-PE. Lipid vesicles rupture on the silica coated (thickness ≈ 10 nm) planar embedded gold nanodisks (p = 400 nm and d = 100 nm). The calculated steady-state time-averaged electric Þeld intensity (E_z^2) is also shown (not to scale). b) Bright Þeld image of a microßuidic chip showing two microßuidic channels (dashed white lines) aligned with the embedded gold nanodisks (darker region). The scale bar is 50 µm. The inset shows a SEM image of the embedded gold nanodisk array. The scale bar is 200 nm. c) LSPR peak shift versus time upon injecting vesicles to the microßuidic channels. The arrow indicates injection of vesicles. d) LSPR peak shift versus time upon injecting SAPE into the channels. The arrow indicates injection of SAPE. e) Fluorescence image of the embedded gold nanodisk array after SAPE injection. The scale bar is 50 µm. f) Extinction spectra (in absorption units) of the planar embedded gold nanodisk array taken at speciÞc time intervals showing the distinct LPSR peak shifts. The inset shows a magniÞed view of the peak shifts.

rupture to form a SLB. Phosphate buffered saline (PBS) washing removed excess vesicles and the peak shift reaches a steady state. The LSPR peak from both channels shifts ≈1.7 nm due to the formation of SLBs. Then we injected bovine serum albumin (BSA) in PBS solution (1 mg/mL) to both channels to minimize non-specific adsorption of SAPE, and the channels were subsequently washed with PBS. A 100 nM SAPE solution was injected to both channels, followed by PBS washing. The SAPE selectively binds to biotin, as is evident by the ≈1.2 nm peak shift only in the biotinylated SLBs in Ch 1 (see Figure 6d). As expected, Ch 2 does not show any binding due to the absence of a binding partner in the SLB. Because the intermediate silica layer prevents quenching of fluorophores on the gold patterns, we can perform LSPR sensing and fluorescence imaging on the same sample. While the primary function of metallic nanodisk array is label-free LSPR biosensing, it is highly desirable to add concurrent fluorescence imaging capability, which would allow cross-checking the molecular binding events as well as perform FRAP measurements on the same sample that is used for LSPR sensing. Furthermore, plasmon-enhanced fluorescence emission can also be utilized for certain applications. However, a direct contact between the fluorophores and the metal surface can lead to fluorescent quenching. In our sensor, the 10 nm silica plays double roles: it acts as a spacer to prevent direct contact between the metallic nanodisks and the fluorophores and also forms a homogenous and hydrophilic platform for SLB formation. Figure 6e shows the fluorescent emission from SAPE, imaged after finishing the LSPR sensing experiment, demonstrating that the SAPE bound only to the biotinylated SLB in Ch 1. The extinction spectra taken at time intervals corresponding to the LSPR peak shifts are shown in Figure 6f. The extinction peaks shift ≈1.7 nm and ≈1.2 nm corresponding to the formation of SLBs and the binding of SAPE, respectively. The LSPR shift of ≈1.2 nm, after SAPE binding, is comparable to earlier reported values.[58]

A surface with protruded nanoparticles has been shown to deform a lipid bilayer which can lead to the formation of pores or an incomplete coverage,[59] and surface topography has shown to affect the adsorption of proteins.[60] The peak shift in LSPR sensors can also change with deformation of the SLB such as the formation of pores, which might occur in the case of protruding nanodisks, especially if the nanodisk surface is rough.[59] We performed 3D FDTD simulations to understand the effect on LSPR shift due to these structural deformations of SLB (see Figure S3 in the Supporting Information). We observed a decrease in the LSPR shift in the case of the pore formation compared to the case where the SLB conformally covers the protruding nanodisks, which is attributed to the fact that there is no SLB formed at the corners of the nanodisks where there is strong plasmon field localization. For the embedded particles,

the SLB conformally covers the top silica surface and hence the LSPR shift will be more reliable.

3. Conclusions

We have demonstrated a template-stripping process for making topographically flat substrates with disconnected metallic structures embedded in optical epoxy or PDMS. Gold nanodisks as small as 100 nm in diameter and less than 30 nm in thickness can be embedded in optical epoxy and peeled off without adhesion layers. The measured roughness and topography of the surface is below 1 nm. The embedded gold nanodisks show resonant plasmonic field enhancement with an EM field decay length of ≈21 nm. The smoothness of the device is maintained after sealing the patterned surface with a 10 nm-thick silica film via ALD. The ultraflat silica overlayer shields the underlying metals, and eliminates the need for chemical functionalization of the metals while presenting a biocompatible surface, which enables a permanent bond with a PDMS microfluidic chip, and prevents quenching of fluorophores due to metals.

This ultraflat LSPR sensing platform with a silica top surface has many potential applications for studying the biophysics of lipid bilayers and cholesterol-rich lipid domains (i.e., lipid rafts). Traditionally, SLBs containing cholesterol-rich domains have been prepared on ultraflat substrates such as mica due to the delicate interplay between membrane curvature and spatial organization.[61] Elimination of substrate and membrane curvature makes high-resolution AFM studies possible where heterogeneous membrane domains are identified by subtle changes in membrane thickness, typically less than 1 nm.[62] Another application of our substrates is for near-field optical microscopy: the topographically flat surface decouples structural artifacts from the optical information; while the embedded metallic particles enhance the optical field collected by the near-field probe.[63] Furthermore, the ultraflat silica surface is amenable to optical, electrical, or microfluidic[51] techniques to manipulate biological objects along the surface and embedding disconnected metallic patterns in PDMS have many interesting applications in stretchable devices.

4. Experimental Section

Fabrication of Gold Nanodisks: A Si wafer was spin-coated with polymethyl methacrylate (PMMA) resist and patterned using electron-beam lithography. The patterns have different hole sizes (d = 100, 120, 140, and 160 nm) and periods (p = 300, 350, and 400 nm). A 27 nm thick gold layer was deposited (rate of 1 • /s) on the pattern using electron-beam evaporation (Temescal). The PMMA resist was released using acetone and the gold nanodisk array was coated by a UV curable epoxy (Norland Optical Adhesive NOA61) with a glass microscope slide as a backing plate. After curing the epoxy under UV light, the gold nanodisks were peeled off from the Si substrate. The fabrication details are illustrated in Figure S1 in the Supporting Information. For template stripping using PDMS, the metallic structures were incubated overnight at room temperature in a vacuum desiccator containing a few drops of 95% 3-mercaptopropyl trimethoxysilane (Sigma-Aldrich), which acted as an adhesion promoter between the metal and PDMS. PDMS was degassed and spin-coated (500 rpm for 6 s) on the functionalized sample and cured overnight at 70 °C, after putting a glass backing slide. The metallic structures embedded in PDMS are then peeled off from the Si substrate.

Optical Extinction Spectroscopy: The samples were illuminated (from the nanodisk side) with a tungsten-halogen lamp and the transmission spectra were collected using a microscope objective lens (10×) and sent to an imaging spectrometer equipped with a deep-cooled low-noise CCD camera (Princeton PIXIS). A grating of 120 lines/mm was used to collect the spectrum in the wavelength range of 400–850 nm. The spectra were collected over the region of the nanodisks and then normalized with that from a bare epoxy surface.

FDTD Simulation: 3D FDTD simulations were performed using the commercial software package FullWAVE (Rsoft Design Group). A unit cell consisting of a single gold nanodisk (optical constants of gold were taken from Rakic et al.[64]) embedded in an epoxy layer (refractive index of 1.56) was modeled by applying periodic boundary conditions in the in-plane dimensions and perfectly matched layer (PML) boundary conditions on the boundaries parallel to the gold-epoxy interfaces. A grid size of 1 nm was chosen in all the three dimensions in the unit cell. For a wavelength spectrum of the nanodisks, a pulsed excitation from the air side of the device was used, and the simulation was run until a steady-state is achieved. For spatial field maps at resonance, a continuous wave excitation was used and the time-averaged total electric field intensity, $E_{total} = E_x^2 + E_y^2 + E_z^2$, was calculated.

Vesicle Preparation: A 1 mM (≈1 mg/mL) lipid mixture (Egg PC, Avanti Polar Lipids), 10 mol% biotin-PE (1,2-dipalmitoyl-sn-glycero-3-phosphoethanolamine-*N*-(biotinyl) (Avanti Polar Lipids) and/or 1 mol% Texas red-dihexadecanoyl-*sn*-glycero-3-phosphoethanolamine (Texas Red-DHPE; Invitrogen) was dried and then rehydrated with Tris buffer (100 mM NaCl, 10 mM Tris, 1 mM ethylenediaminetetraacetic acid (EDTA), pH 8.0) to form vesicles with a wide distribution of sizes. These vesicles were sonicated for 10 min and extruded (15 passes) using a polycarbonate filter, with 200 nm pore diameter. The vesicles were mixed with Tris calcium buffer (100 mM NaCl, 10 mM Tris, 10 mM $CaCl_2$, pH 8.0) prior to LSPR sensing experiments.

Time-Resolved LSPR Kinetic Sensing with SLBs and SAPE: A 10 nm-thick silica layer was deposited on an embedded gold nanodisk sample, with an array area of 40 μm × 40 μm (p = 400 nm and d = 100 nm). A PDMS microfluidic chip with two microfluidic channels each with 100 μm width and 50 μm height were aligned and permanently bonded to the nanodisk array. Both channels were washed with PBS for about an hour. A constant flow rate of 12 μL/min was maintained throughout the experiment, unless otherwise mentioned. After a 5 min of stable PBS base line, 1 mM biotinylated vesicles (10 mol% biotin) were injected into channel 1 at a flow rate of 5 μL/h. As a negative control experiment, vesicles without biotin-PE were injected into channel 2. The optical extinction spectra were collected using a microscope objective lens (4×) and sent to an imaging spectrometer coupled with a CCD and recorded every 2.4 s. The spectral shift of the extinction peak around 775 nm was monitored. PBS washing for about 90 min removed excess vesicles. Before injecting SAPE, BSA in PBS solution (1 mg/mL) was injected to prevent non-specific adsorption of SAPE, and the channels were subsequently washed with PBS. After washing the channels with PBS for 12 min, a 100 nM SAPE solution was injected for 10 min, followed by PBS washing for about 90 min. Fluorescence imaging of the SAPE (fluorophore phycoerythrin, maximum absorption at ≈565 nm, maximum emission at ≈578 nm) was carried out using a halogen lamp with 540–553 nm excitation filter and 565–605 nm emission filter.

Fluorescence Recovery After Photobleaching (FRAP) Experiments: The vesicles spontaneously rupture on a silica-coated (≈10 nm thick) template-stripped epoxy surface to form a SLB. After vesicle rupture, the substrate was imaged using an upright confocal microscope. A small circular spot (radius ≈ 10 μm) on the SLBs was photobleached with simultaneous laser beams at 405, 488, and 543 nm for 10 s. Fluorescence recovery of the photobleached area on the surface was monitored by imaging with a 543 nm laser spot over the sample at a rate of 0.5 Hz. The FRAP analysis is given in the Supporting Information.

Supporting Information

Supporting Information is available from the Wiley Online Library or from the author.

Acknowledgements

This work was supported by grants to S.-H.O. from the National Science Foundation (NSF CAREER Award, DBI 0964216, and DMR 0941537), Office of Naval Research Young Investigator Award (N00014-11-1-0645), National Institutes of Health (R01 GM092993), and Minnesota Partnership Award for Biotechnology. Parts of this work were carried out in the Characterization Facility, University of Minnesota, which receives partial support from the NSF through the MRSEC program. Device fabrication was performed at the University of Minnesota Nanofabrication Center, which receives support from the NSF through the National Nanotechnology Infrastructure Network. L.R.J acknowledges support from a 3M fellowship. T.W.J. acknowledges support from the NIH biotechnology training grant. S.H.O. also acknowledges support from the WCU Program #R31-10032 funded by the Ministry of Education, Science & Technology and the National Research Foundation of Korea.

Received: August 6, 2012
Revised: October 18, 2012
Published online: January 15, 2013

[1] W. L. Barnes, A. Dereux, T. W. Ebbesen, *Nature* **2003**, *424*, 824.
[2] H. T. Miyazaki, Y. Kurokawa, *Phys. Rev. Lett.* **2006**, *96*, 097401.
[3] H. A. Atwater, *Sci. Am.* **2007**, *296*, 56.
[4] L. Novotny, N. F. van Hulst, *Nat. Photonics* **2011**, *5*, 83.
[5] A. D. McFarland, R. P. Van Duyne, *Nano Lett.* **2003**, *3*, 1057.
[6] A. G. Brolo, R. Gordon, B. Leathem, K. L. Kavanagh, *Langmuir* **2004**, *20*, 4813.
[7] A. B. Dahlin, M. ZŠch, T. Rindzevicius, M. KŠll, D. S. Sutherland, F. Hšsk, *J. Am. Chem. Soc.* **2005**, *127*, 5043.
[8] M. E. Stewart, N. H. Mack, V. Malyarchuk, J. A. N. T. Soares, T. W. Lee, S. K. Gray, R. G. Nuzzo, J. A. Rogers, *Proc. Natl. Acad. Sci. USA* **2006**, *103*, 17143.
[9] A. Lesuffßeur, H. Im, N. C. Lindquist, S.-H. Oh, *Appl. Phys. Lett.* **2007**, *90*, 243110.
[10] L. Pang, G. M. Hwang, B. Slutsky, Y. Fainman, *Appl. Phys. Lett.* **2007**, *91*, 123112.
[11] H. Gao, J.-C. Yang, J. Y. Lin, A. D. Stuparu, M. H. Lee, M. Mrksich, T. W. Odom, *Nano Lett.* **2010**, *10*, 2549.
[12] J. W. Menezes, J. Ferreira, M. J. L. Santos, L. Cescato, A. G. Brolo, *Adv. Funct. Mater.* **2010**, *20*, 3918.
[13] C. L. Haynes, A. McFarland, R. P. Van Duyne, *Anal. Chem.* **2005**, *77*, 338A.
[14] M. L. Juan, R. Gordon, Y. Pang, F. Eftekhari, R. Quidant, *Nat. Phys.* **2009**, *5*, 915.
[15] W. A. Challener, C. Peng, A. V. Itagi, D. Karns, W. Peng, Y. Peng, X. Yang, X. Zhu, N. J. Gokemeijer, Y. T. Hsia, G. Ju, R. E. Rottmayer, M. A. Seigler, E. C. Gage, *Nat. Photonics* **2009**, *3*, 220.
[16] W. Sparreboom, A. van den Berg, J. C. T. Eijkel, *New J. Phys.* **2010**, *12*, 015004.
[17] Y. B. Zheng, J. L. Payton, T. B. Song, B. K. Pathem, Y. Zhao, H. Ma, Y. Yang, L. Jensen, A. K. Y. Jen, P. S. Weiss, *Nano Lett.* **2012**, *12*, 5362.
[18] B. Hecht, H. Bielefeldt, Y. Inouye, D. Pohl, L. Novotny, *J. Appl. Phys.* **1997**, *81*, 2492.
[19] T. Kalkbrenner, M. Graf, C. Durkan, J. Mlynek, V. Sandoghdar, *Appl. Phys. Lett.* **2000**, *76*, 1206.
[20] Y. Roiter, M. Ornatska, A. R. Rammohan, J. Balakrishnan, D. R. Heine, S. Minko, *Nano Lett.* **2008**, *8*, 941.
[21] W. J. Galush, S. A. Shelby, M. J. Mulvihill, A. Tao, P. Yang, J. T. Groves, *Nano Lett.* **2009**, *9*, 2077.
[22] L. He, J. W. F. Robertson, J. Li, I. Karcher, S. M. Schiller, W. Knoll, R. Naumann, *Langmuir* **2005**, *21*, 11666.
[23] P. Zijlstra, J. W. M. Chon, M. Gu, *Nature* **2009**, *459*, 410.
[24] T. W. Ebbesen, C. Genet, S. I. Bozhevolnyi, *Phys. Today* **2008**, *61*, 44.
[25] D. S. Gray, J. Tien, C. S. Chen, *Adv. Mater.* **2004**, *16*, 393.
[26] N. C. Lindquist, P. Nagpal, K. M. McPeak, D. J. Norris, S.-H. Oh, *Rep. Prog. Phys.* **2012**, *75*, 036501.
[27] D. Hausmann, J. Becker, S. Wang, R. G. Gordon, *Science* **2002**, *298*, 402.
[28] H. Im, N. J. Wittenberg, A. Lesuffßeur, N. C. Lindquist, S.-H. Oh, *Chem. Sci.* **2010**, *1*, 688.
[29] M. Hegner, P. Wagner, G. Semenza, *Surf. Sci.* **1993**, *291*, 39.
[30] R. Naumann, S. M. Schiller, F. Giess, B. Grohe, K. B. Hartman, I. KŠrcher, I. Kšper, J. LŸbben, K. Vasilev, W. Knoll, *Langmuir* **2003**, *19*, 5435.
[31] J. C. Love, L. A. Estroff, J. K. Kriebel, R. G. Nuzzo, G. M. Whitesides, *Chem. Rev.* **2005**, *105*, 1103.
[32] C.-H. Sun, N. C. Linn, P. Jiang, *Chem. Mater.* **2007**, *19*, 4551.
[33] P. Nagpal, N. C. Lindquist, S.-H. Oh, D. J. Norris, *Science* **2009**, *325*, 594.
[34] N. C. Lindquist, P. Nagpal, A. Lesuffßeur, D. J. Norris, S.-H. Oh, *Nano Lett.* **2010**, *10*, 1369.
[35] J.-C. Yang, H. Gao, J. Y. Suh, W. Zhou, M. H. Lee, T. W. Odom, *Nano Lett.* **2010**, *10*, 3173.
[36] N. Vogel, M. Jung, N. L. Bocchio, M. Retsch, M. Kreiter, I. Koper, *Small* **2010**, *6*, 104.
[37] J. Jose, F. B. Segerink, J. P. Korterik, A. Gomez-Casado, J. Huskens, J. L. Herek, H. L. Offerhaus, *J. Appl. Phys.* **2011**, *109*, 064906.
[38] W. Zhou, T. W. Odom, *Nat. Nanotechnol.* **2011**, *6*, 423.
[39] N. Vogel, J. Zieleniecki, I. Kšper, *Nanoscale* **2012**, *4*, 3820.
[40] S. H. Lee, T. W. Johnson, N. C. Lindquist, H. Im, D. J. Norris, S.-H. Oh, *Adv. Funct. Mater.* **2012**, *22*, 4439.
[41] N. C. Lindquist, T. W. Johnson, D. J. Norris, S.-H. Oh, *Nano Lett.* **2011**, *11*, 3526.
[42] K. J. Lee, K. A. Fosser, R. G. Nuzzo, *Adv. Funct. Mater.* **2005**, *15*, 557.
[43] D. Chanda, K. Shigeta, S. Gupta, T. Cain, A. Carlson, A. Mihi, A. J. Baca, G. R. Bogart, P. Braun, J. A. Rogers, *Nat. Nanotechnol.* **2011**, *6*, 402.
[44] T.-Y. Yoon, C. Jeong, S.-W. Lee, J. H. Kim, M. C. Choi, S.-J. Kim, M. W. Kim, S.-D. Lee, *Nat. Mater.* **2006**, *5*, 281.
[45] M. Jung, N. Vogel, I. Koper, *Langmuir* **2011**, *27*, 7008.
[46] E. Reimhult, F. Hšsk, B. Kasemo, *Langmuir* **2003**, *19*, 1681.
[47] M. P. Jonsson, P. Jšnsson, A. B. Dahlin, F. Hšsk, *Nano Lett.* **2007**, *7*, 3462.
[48] E. T. Castellana, P. S. Cremer, *Surf. Sci. Rep.* **2006**, *61*, 429.
[49] X. Zhang, J. Zhao, A. V. Whitney, J. W. Elam, R. P. Van Duyne, *J. Am. Chem. Soc.* **2006**, *128*, 10304.
[50] H. Im, N. C. Lindquist, A. Lesuffßeur, S.-H. Oh, *ACS Nano* **2010**, *4*, 947.
[51] P. Jšnsson, M. P. Jonsson, F. Hšsk, *Nano Lett.* **2010**, *10*, 1900.
[52] B. Lamprecht, G. Schider, R. Lechner, H. Ditlbacher, J. Krenn, A. Leitner, F. R. Aussenegg, *Phys. Rev. Lett.* **2000**, *84*, 4721.
[53] K. A. Willets, R. P. Van Duyne, *Annu. Rev. Phys. Chem.* **2007**, *58*, 267.
[54] A. J. Haes, R. P. Van Duyne, *Anal. Bioanal. Chem.* **2004**, *379*, 920.
[55] S. Chen, M. Svedendahl, M. KŠll, L. Gunnarsson, A. Dmitriev, *Nanotechnology* **2009**, *20*, 434015.
[56] P. Jšnsson, M. P. Jonsson, J. O. Tegenfeldt, F. Hšsk, *Biophys. J.* **2008**, *95*, 5334.
[57] K. J. Seu, A. P. Pandey, F. Haque, E. A. Proctor, A. E. Ribbe, J. S. Hovis, *Biophys. J.* **2007**, *92*, 2445.

[58] H. Im, S. H. Lee, N. J. Wittenberg, T. W. Johnson, N. C. Lindquist, P. Nagpal, D. J. Norris, S.-H. Oh, *ACS Nano* **2011**, *5*, 6244.
[59] Y. Roiter, M. Ornatska, A. R. Rammohan, J. Balakrishnan, D. R. Heine, S. Minko, *Langmuir* **2009**, *25*, 6287.
[60] C. Galli, M. Collaud Coen, R. Hauert, V. L. Katanaev, P. Gršning, L. Schlapbach, *Colloids Surf. B* **2002**, *26*, 255.
[61] R. Parthasarathy, J. T. Groves, *Soft Matter* **2007**, *3*, 24.
[62] E. I. Goksu, J. M. Vanegas, C. D. Blanchette, W.-C. Lin, M. L. Longo, *Biochim. Biophys. Acta* **2009**, *1788*, 254.
[63] J. Krenn, A. Dereux, J. Weeber, E. Bourillot, Y. Lacroute, J. Goudonnet, G. Schider, W. Gotschy, A. Leitner, F. R. Aussenegg, C. Girard, *Phys. Rev. Lett.* **1999**, *82*, 2590.
[64] A. D. Rakic, A. B. Djurišic, J. M. Elazar, M. L. Majewski, *Appl. Opt.* **1998**, *37*, 5271.